EVOLUTION OF THE SYNCHROTRON SPECTRUM IN MARKARIAN 421 DURING THE 1998 CAMPAIGN

Chiharu Tanihata,[1,2] Jun Kataoka,[3] Tadayuki Takahashi,[1,2] and Greg M. Madejski[4]

ABSTRACT

The uninterrupted 7 day *ASCA* observations of the TeV blazar Mrk 421 in 1998 have clearly revealed that X-ray flares occur repeatedly. In this paper, we present the results of the time-resolved spectral analysis of the combined data taken by *ASCA*, *RXTE*, *BeppoSAX*, and the *Extreme Ultraviolet Explorer* (*EUVE*). In this object—and in many other TeV blazars—the precise measurement of the shape of the X-ray spectrum, which reflects the high-energy portion of the synchrotron component, is crucial in determining the high-energy cutoff of the accelerated electrons in the jet. Thanks to the simultaneous broadband coverage, we measured the 0.1–25 keV spectrum resolved on timescales as short as several hours, providing a great opportunity to investigate the detailed spectral evolution at the flares. By analyzing the time-subdivided observations, we parameterize the evolution of the synchrotron peak, where the radiation power dominates, by fitting the combined spectra with a quadratic form [where the νF_ν flux at the energy E obeys $\log \nu F_\nu(E) = \log\left(\nu F_{\nu,\,\mathrm{peak}}\right) - \mathrm{const}\left(\log E - \log E_{\mathrm{peak}}\right)^2$]. In this case, we show that there is an overall trend that the peak energy E_{peak} and peak flux $\nu F_{\nu,\,\mathrm{peak}}$ increase or decrease together. The relation of the two parameters is best described as $E_{\mathrm{peak}} \propto \nu F_{\nu,\,\mathrm{peak}}^{0.7}$ for the 1998 campaign. Similar results were derived for the 1997 observations, while the relation gave a smaller index when both 1997 and 1998 data were included. On the other hand, we show that this relation, and also the detailed spectral variations, differs from flare to flare within the 1998 campaign. We suggest that the observed features are consistent with the idea that flares are due to the appearance of a new spectral component. With the availability of the simultaneous TeV data, we also show that there exists a clear correlation between the synchrotron peak flux and the TeV flux.

Subject headings: BL Lacertae objects: individual (Markarian 421) — galaxies: active — radiation mechanisms: nonthermal — X-rays: galaxies

1. INTRODUCTION

The uninterrupted 7 day *ASCA* observation of the TeV blazar Mrk 421 in 1998 has revealed that day-scale X-ray flares seen in previous observations were probably unresolved superpositions of many smaller flares (Takahashi et al. 2000). The nearly continuous observation allowed not only the possibility of tracking the individual flares entirely from the rise to decay, but it also enabled quantitative statistical tests of the time series by employing the power spectrum or the structure function (Kataoka et al. 2001; Tanihata et al. 2001).

The main characteristic of blazars is their high flux observed from radio to γ-rays, coupled with strong variability and strong polarization. These properties are now successfully explained by the scenario in which blazars are active galactic nuclei (AGNs) possessing jets aligned close to the line of sight and, accordingly, the Doppler-boosted nonthermal emission from the jet dominates other emission components (e.g., Blandford & Königl 1979; Urry & Padovani 1995). This is what makes blazars critical in understanding jets in AGNs.

The broadband spectra of blazars consist of two peaks, one in the radio-to–optical-UV range (and in some cases, reaching to the X-ray band) and the other in the hard X-ray–to–γ-ray region. The high polarization of the radio-to-optical emission suggests that the lower energy peak is produced via the synchrotron process by relativistic electrons in the jet. The higher energy peak is believed to be due to Compton upscattering of seed photons by the same population of relativistic electrons. Several possibilities exist for the source of the seed photons; these can be the synchrotron photons internal to the jet (Jones, O'Dell, & Stein 1974; Ghisellini & Maraschi 1989), but they can also be external, such as from the broad emission line clouds (Sikora, Begelman, & Rees 1994) or the accretion disk (Dermer, Schlickeiser, & Mastichiadis 1992; Dermer & Schlickeiser 1993).

The blazars with peak synchrotron output in the X-ray range also emit strongly in the γ-ray energies, and the brightest of those have been detected in the TeV range with ground-based Cerenkov arrays. These are the so-called TeV blazars. In TeV blazars, variability of the synchrotron flux is measured to be the strongest and most rapid in the X-ray band, and thus it provides the best opportunity to study the electrons that are accelerated to the highest energies. In particular, the synchrotron peak is a very important observable in two aspects: first, because the flux at the peak represents the total emitted power from the blazar and second, because the peak frequency reflects the maximum energy of radiating particles gained in the acceleration process.

Mrk 421 is among the closest known blazars, at a redshift of 0.031, and it was the first blazar (and also the first extragalactic source) discovered to be a TeV emitter. It was first detected as a weak source by EGRET (Lin et al. 1992), and 9 months later, Whipple detected a clear signal from this object between 0.5 and 1.5 TeV (Punch et al. 1992; Petry et al. 1996). Flux variability on various timescales has been observed,

[1] Institute of Space and Astronautical Science, 3-1-1 Yoshinodai, Sagamihara 229-8510, Japan; tanihata@astro.isas.ac.jp.

[2] Department of Physics, University of Tokyo, 7-3-1 Hongo, Bunkyo-ku, Tokyo 113-0033, Japan.

[3] Department of Physics, Tokyo Institute of Technology, Tokyo 152-8551, Japan.

[4] Stanford Linear Accelerator Center, Stanford, CA 94309-4349.

including a very short flare with a duration of ~ 1 hr (Gaidos et al. 1996). Ever since, Mrk 421 has been repeatedly confirmed to be a TeV source by various ground-based telescopes. It has also been one of the most studied blazars and a target of several multiwavelength campaigns (Macomb et al. 1995; Maraschi et al. 1999; Takahashi et al. 2000).

The multiwavelength campaign of Mrk 421 in 1998 was one of the first opportunities to observe a blazar in the TeV range using several telescopes located in different locations in the world, so as to have coverage as continuous as possible (Aharonian et al. 1999; Piron et al. 2001). Observations in other frequencies included X-ray observations by *ASCA*, *RXTE* (Takahashi et al. 2000), and *BeppoSAX* (Maraschi et al. 1999; Fossati et al. 2000a, 2000b), EUV observations by the *Extreme Ultraviolet Explorer* (*EUVE*), optical observation with *BVRI* filters organized by the WEBT collaboration,[5] and radio observations at the Metsähovi Radio Observatory.

In this paper, we present the results of the spectral analysis of X-ray and EUV data during the 1998 April campaign. In particular, we estimate the location of the synchrotron peak in the νF_ν spectrum. So far, quantitative studies of the variation of the synchrotron peak have been conducted only for the two brightest blazars, Mrk 421 and Mrk 501. The largest variation of the synchrotron peak energy was observed in Mrk 501 by *BeppoSAX*; the peak energy shifted ~ 2 orders of magnitude (Pian et al. 1998). Collecting data from different epochs (separated by as much as ~ 2 yr), Tavecchio et al. (2001) have shown a relation of the form $E_{\rm peak} \propto F_{0.1-100\,\rm keV}^n$, with $n \geq 2$. A similar analysis was done by Fossati et al. (2000b) for the Mrk 421 data obtained by *BeppoSAX* in 1997 and 1998, showing a relation of $E_{\rm peak} \propto F_{0.1-10\,\rm keV}^n$, with $n = 0.55$. In this paper we describe a continuous 7 day variation of the synchrotron peak, which allows us to investigate the dynamical change of the synchrotron spectrum during the flares.

We first describe the observations and data analysis in § 2. The results of spectral analysis are described in § 3; a summary of the results and a discussion of our findings, with emphasis on the temporal evolution of the spectrum, are presented in § 4.

2. OBSERVATION AND DATA ANALYSIS

The week-long multifrequency campaign of Mrk 421 was carried out in 1998 April (Takahashi et al. 2000). The goal of this paper is to study the evolution of the high-energy synchrotron spectrum as a function of time during the campaign and also the correlation with the TeV flux. This requires the best possible spectral coverage in the X-ray range, for which we assembled all available data collected during the campaign, including pointings by X-ray observatories *ASCA*, *RXTE*, and *BeppoSAX*, as well as EUV observations by *EUVE*.

2.1. *ASCA*

Mrk 421 was observed continuously with *ASCA* for 7 days (except for the Earth occultation), 1998 April 23.97–30.8 UT (PI: T. Takahashi). The *ASCA* detectors—two SISs (Solid State Imaging Spectrometers; Burke et al. 1991; Yamashita et al. 1997) and two GISs (Gas Imaging Spectrometers; Ohashi et al. 1996)—were in operation. We refer to Tanihata et al. (2001) for the details of the observation modes and data reduction. The obtained spectra were rebinned so that all bins have the same statistics.

Since late 1994, the efficiency of both SIS detectors below ~ 1 keV has been decreasing over time. The problem is believed to be caused by the increased residual dark current level and also by the decrease in the charge transfer efficiency, although an effort is still underway to model the effects. While it has been reported that it may be possible to parameterize the degradation by an additional absorption column as a function of time (Yaqoob et al. 2000), since our observation concerns the precise shape of the continuum spectrum, we used only the data obtained by the GISs for spectral analysis. (Note that the X-ray spectra in Fig. 2 of Takahashi et al. 2000 show the data obtained by the SISs. Because the SISs were used, there is too strong a decrease of inferred flux at the lower energy, which is due to instrumental effects described above.)

2.2. *RXTE*

The *RXTE* observations (PI: G. M. Madejski) were mainly coordinated to coincide with the *ASCA* observation period but were conducted, mostly, only during the low-background orbits. The *RXTE* extends the *ASCA* bandpass to a higher energy with the PCA (Proportional Counter Array; 2–60 keV) and HEXTE (High Energy X-Ray Timing Experiment; 15–200 keV) instruments. However, because both the flux from the source and the sensitivities of the detectors decrease toward higher energies, in the analysis below we use only the data from the PCA, in the energy range 3–25 keV.

All data reduction was performed using the HEASOFT software packages, based on the REX script, provided by the *RXTE* Guest Observer Facility (GOF). The screening criteria excluded data from times when the elevation angle from the Earth's limb was lower than $10°$ and data acquired during the South Atlantic Anomaly (SAA) passages. Since the Proportional Counter Units (PCUs) are activated during the SAA passage, we used the data only from times after the background level had dropped to the quiescent level and become stable, typically 30 minutes after the peak of an SAA passage.

For the best signal-to-noise ratio, we selected events only from the top xenon layer and excluded events from other gas layers. For maximum consistency among the observations, we used only the three detectors that were turned on for all the observations (known as PCU0, PCU1, and PCU2). Since the PCA is not an imaging detector, blank-sky observations must be used to estimate the background spectrum. For these, we used the background models provided by the *RXTE* GOF to evaluate the background during each observation. We note that the residual background contamination of the data within the energy bandpass we selected was always significantly lower than the source counts. The mean net *RXTE* PCA count rate from Mrk 421 in the 10–20 keV range for the three PCUs named above was at least ~ 3 counts s^{-1}, while the total residuals from the blank sky in this energy range *plus* the fluctuations of the cosmic X-ray background were lower than 0.2 counts s^{-1} (see the HEASARC Web site regarding the *RXTE* PCA background), providing confidence that an imprecise background subtraction did not affect our results.

2.3. *BeppoSAX*

The *BeppoSAX* observations (PI: L. Chiappetti) started 3 days before the *ASCA* observations (Maraschi et al. 1999; Fossati et al. 2000a, 2000b). We use the data obtained by the LECS (Low Energy Concentrator Spectrometer; 0.1–10 keV), which extends the bandpass to a lower energy, and also the MECS (Medium Energy Concentrator Spectrometer; 1.3–10 keV).

The data analysis was based on the linearized event files, together with the appropriate background event files and response matrices, provided by the *BeppoSAX* Science Data Center (SDC). Data reduction was performed using the standard HEASOFT software, XSELECT.

We extracted the source photons from a circular region centered at the source with a radius of 8′ for both LECS and MECS. For the background photons, we constructed the spectra by extracting the photons from the same detector regions, using blank-sky observations. Each spectrum was rebinned using the grouping templates provided by the *BeppoSAX* SDC, and we limited the energy range to 0.12–4.0 keV for LECS and 1.65–10.5 keV for MECS, as suggested in the Handbook for *BeppoSAX* NFI Spectral Analysis (Fiore, Guainazzi, & Grandi 1999).[6]

2.4. *EUVE*

The *EUVE* observations covered the entire campaign of Mrk 421 from April 19.4 to May 1.2 (PI: T. Takahashi). The source photons were extracted in a 12′ aperture. In order to estimate the absolute flux in the EUV range, we normalized it to be consistent with the data obtained simultaneously by the other observatories. Given that the EUV spectrum is difficult to determine within the rather limited bandpass, we used only the observed integrated count rate (see Marshall, Fruscione, & Carone 1995). For this, we used the period when the observations by all observatories overlapped (MJD 50,927.03–50,927.34; § 3.1). During this period, the average *EUVE* count rate was 0.46 ± 0.01 counts s^{-1}. At the same time, the 0.13–0.18 keV flux derived from the combined LECS, MECS, GIS, and PCA spectrum gives $\nu F_\nu = (1.78 \pm 0.04) \times 10^{-10}$ ergs cm^{-2} s^{-1}, where the error represents the statistical error.

An additional uncertainty arises from the fact that the difference in the spectral shape is not taken into account. This can be estimated from the results in Marshall et al. (1995). Taking $N_H = 1.5 \times 10^{20}$ cm^{-2} for Mrk 421, assuming that the spectrum index varies from 0.5 to 1.0, the flux density would vary from 1363 to 1394 μJy for 1 count s^{-1} in the *EUVE* range. This gives an additional 2.5% error as a systematic error.

In the following analysis, we use the above value for scaling the observed *EUVE* count rate to flux. Thus,

$$\nu F_\nu(EUVE) = 1.78 \times 10^{-10} \left(\frac{F_{\text{cts s}^{-1}}}{0.46} \right) \text{ ergs s}^{-1} \text{ cm}^{-2}, \quad (1)$$

where $F_{\text{cts s}^{-1}}$ is the *EUVE* count rate.

3. RESULTS

3.1. *The Shape of the* 0.1–25 keV *Spectrum*

During April 24, observations by all three X-ray satellites, *ASCA*, *BeppoSAX*, *RXTE*, and also *EUVE* happened to exactly overlap continuously for 26.5 ks (MJD 50,927.03–50,927.34). This provides us with high-quality data over a very broad energy coverage, spanning more than 2 decades, from 0.12 to 25 keV. The net exposures during the overlapping 26.5 ks period were 9.1, 13.3, 3.6, and 5.5 ks for GIS, PCA, LECS, and MECS, respectively.

We first fitted the spectrum for each instrument with a power-law model, with a low-energy absorption fixed to the

Galactic value, $N_H = 1.5 \times 10^{20}$ cm^{-2} (Elvis, Lockman, & Wilkes 1989). The results are shown in the top half of Table 1, suggesting that the fit is not adequate for any of the individual instruments. This certainly suggests that a more complex model, rather than just a simple power-law function, is required to describe the spectrum.

The shape of the synchrotron spectrum is determined from the energy distribution of the radiating electrons, which cuts off at the high energy representing the acceleration limit. As described in § 1, the high-energy end of the synchrotron spectrum in TeV blazars is located in the X-ray range; this is most likely the reason that the high-quality X-ray data cannot be described by a single power law.

Given the curved spectrum for each instrument, we fitted the combined X-ray spectrum with various functions to model the shape of the observed curvature. We note that our aim is not to develop the shape of the curvature from first principles but rather to reproduce the observed data. For this reason, we considered the following models for comparison: (1) a broken power law, (2) a curved power law, (3) a power law with an exponential cutoff, and (4) a quadratic function in the log ν–log(νF_ν) plane. The curved power law that we define below is similar to the broken power law, but the change in the spectral index is not discrete. The form we attempt is $F(E) = KE^{-\Gamma_1}[1 + (E/E_{\text{br}})]^{-\Gamma_2}$. The form for the exponentially cut off power law is $F(E) = KE^{-\Gamma_1} \exp(-E/E_{\text{br}})$, and the quadratic function is described as $\log(\nu F_\nu)(E) = \log(\nu F_{\nu, \text{peak}}) - a(\log E - \log E_{\text{peak}})^2$.

Since there are slight differences in the cross-calibration between the instruments, we allow the normalization to vary for each instrument. For all results below, the flux is normalized to the GIS value, unless otherwise noted. The N_H is fixed to the Galactic value.

By fitting the spectrum with the models above, we first found that the power law with an exponential cutoff is not a good representation of the data: the model cutoff is too sharp at high energies. The broken power law is also not acceptable, and the curved power law is significantly better. We also find that the quadratic function fits the spectrum surprisingly well. The fitted spectra and the residuals to the quadratic model are shown in Figure 1, where all LECS, MECS, GIS, and PCA spectra are shown to be well described with this single function. The results of the spectral fits by the four models are summarized in the bottom half of Table 1.

3.2. *The Time-resolved Spectra*

The *EUVE* observation covered the whole campaign (April 19.4–May 1.2) and thus completely overlapped our 7 day *ASCA* observation. This adds a data point at 0.13–0.18 keV, in addition to the *ASCA* spectrum in the 0.7–7 keV range, providing us the best opportunity to study the continuous spectral variability. In fact, this is the longest continuous monitoring of this object so far, spanning the 0.13–7 keV range.

We divided the whole observation into shorter segments, with each having a duration of 10 ks. In order to combine the GIS and *EUVE* data, the GIS count rate spectra must first be converted to the source flux spectra, as the *EUVE* count rate data convert directly into flux (§ 2.4). For this, we first fitted the GIS spectrum with a curved power-law model with Galactic absorption. This gives the source spectrum in the GIS energy range. Note that this procedure depends on the selected model, but as long as it describes the spectrum well, this should introduce the smallest possible bias. We then combined

TABLE 1
Results of Spectral Fits for Mrk 421 during MJD 50,927.03–50,927.34

Instrument	Energy Range[a] (keV)	Model	Γ_1[b]	Γ_2[b]	E_{br} (keV)	E_{peak} (keV)	$\nu F_{\nu,\,peak}$ (10^{-12} ergs cm^{-2} s^{-1})	a[c]	χ_ν^2 (dof)
LECS................	0.12–4	Power law	2.20 ± 0.01	...	...	...	...	...	2.85 (83)
MECS...............	1.65–10.5	Power law	2.76 ± 0.02	...	...	...	...	...	1.28 (193)
GIS..................	0.7–7	Power law	2.52 ± 0.01	...	...	...	...	...	1.29 (124)
PCA..................	3–25	Power law	2.91 ± 0.01	...	...	...	...	...	2.63 (50)
LECS, MECS, GIS, PCA......	...	Broken Power law	2.21 ± 0.01	2.90 ± 0.01	2.24 ± 0.04	...	...	...	1.86 (451)
LECS, MECS, GIS, PCA......	...	Curved Power law[d]	1.77 ± 0.04	1.66 ± 0.03	2.5 ± 0.3	...	...	...	1.08 (451)
LECS, MECS, GIS, PCA......	...	Cutoff Power law[e]	2.17 ± 0.01	...	7.80 ± 0.14	...	...	...	1.74 (452)
LECS, MECS, GIS, PCA......	...	Quadratic[c]	...	...	...	0.47 ± 0.02	217 ± 3	0.42 ± 0.01	1.07 (452)

Note.—All errors represent the 1 σ error.
[a] Energy range used in the spectral fitting.
[b] Photon index.
[c] $\log(\nu F_\nu)(E) = \log\left(\nu F_{\nu,\,peak}\right) - a\left(\log E - \log E_{peak}\right)^2$.
[d] $F(E) = KE^{-\Gamma_1}\left[1 + (E/E_{br})\right]^{-\Gamma_2}$.
[e] $F(E) = KE^{-\Gamma_1} \exp(-E/E_{br})$.

this with the *EUVE* data, which gives the combined source spectrum.

In fitting the combined *EUVE*/GIS spectra, we first started with a single–power-law model. In similarity to the results in § 3.1, none of the 56 spectra could be fitted with a single–

power-law function, implying the curvature of the spectra, with their average χ_ν^2 of 7.7, for all data sets. Given that a quadratic model fits the spectrum equally well as the curved power-law model, but with fewer parameters (see § 3.1), we assume the quadratic model for all data sets hereafter. In fact,

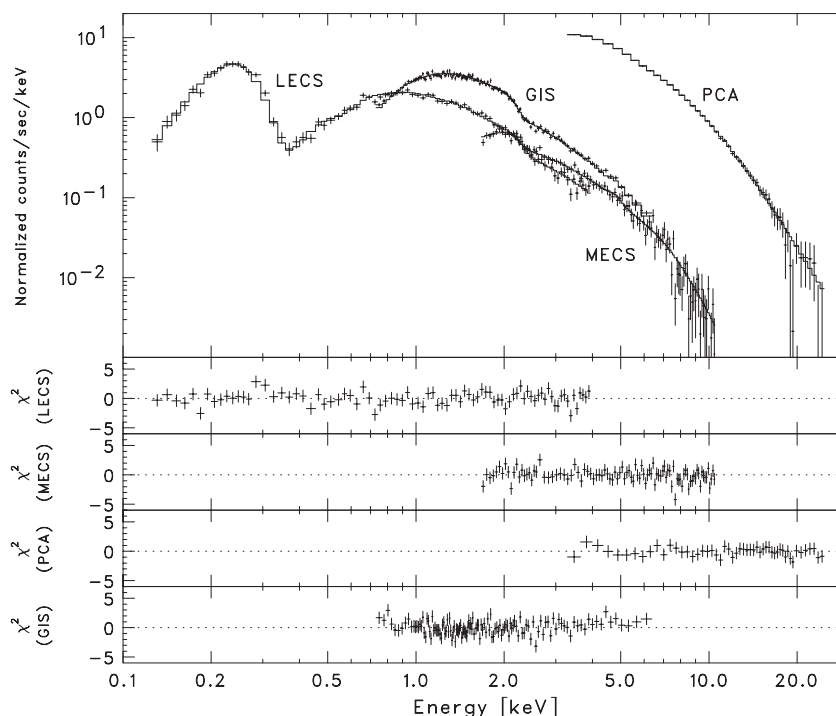Fig. 1.—Joint fit with a quadratic function to the LECS, MECS, GIS, and PCA spectra during the period when the *ASCA*, *BeppoSAX*, and *RXTE* observations overlapped (MJD 50,927.03–50,927.34). The top panel shows the photon spectrum for each instrument. The solid line shows the best-fit model. The bottom four panels shows the residuals of the observed data to the model. See Table 1 for the values of the fit parameters.

because of the energy gap between the *EUVE* and GIS, the fit with a curved power-law model resulted in multiple minima in the χ^2 plane (since the parameters are correlated), and the exact value of the best-fit parameters depended highly on the initial value.

We checked whether the fit was adequate for all data segments. The χ_ν^2 for each fit (Fig. 2, *bottom panel*) ranged from 0.71 to 1.45. The number of degrees of freedom ranged from 60 to 187, which gave $P(\chi^2) > 5\%$ for 53 out of the total of 56 data points. For the other three data points (corresponding to times 230–240, 270–280, and 450–460 ks), we found several line or edgelike structures in the spectra, which resulted in an increase of the χ_ν^2. Although it is not clear whether this is due to some systematic effect or is a true property of the source, since our aim is to model the continuum spectrum correctly, we excluded the energy ranges where those features are present. This improved the fit significantly (*plus signs*). With this, all 56 spectra were well described with the quadratic function.

The time evolution of the derived parameters in the fit is shown in the top three panels in Figure 2: the peak flux, peak energy, and the curvature parameter a (see definition in Table 1). The peak energy is observed to shift between 0.5 and 1.2 keV, where a general trend is found such that the peak energy is higher when the peak flux is higher. This is plotted as the filled circles in Figure 3. The fit results are listed in Table 2.

We do note that the actual validity of using a quadratic function in the entire 0.1–25 keV range was checked in detail (including an examination of trends in residuals) only for the

FIG. 3.—Correlation of the synchrotron peak flux and peak energy for Mrk 421, assuming a quadratic function. Results derived from the combined *EUVE* and *ASCA* spectra during the 1998 campaign are shown as the filled circles. Results from the *BeppoSAX* spectra from the 1998 campaign and 1997 observation are shown as the open circles and squares, respectively. The fluxes for the *BeppoSAX* data are multiplied by a factor of 1.07 to normalize them to the *ASCA* fluxes. Each data point corresponds to the value derived from a spectrum integrated over 10 ks.

epoch when the overlapping *BeppoSAX*, *ASCA*, and *RXTE* observations were available. Since we measured only the *EUVE* flux below 0.7 keV in the combined *EUVE*/GIS fit, the derived peak location can depend on the model function we assume. For instance, if *any* function were allowed, the peak could be located at any energy within the gap. For this reason, we emphasize that the derived peak location is the estimated peak, assuming that the spectrum gap can be extrapolated with the same quadratic function, and also that the error bar describes only the statistical error.

We also analyzed the *BeppoSAX* data during the campaign. Furthermore, in order to make a comparison with data obtained from another campaign, we also analyzed the *BeppoSAX* data obtained in 1997 (PIs: G. Vacanti and L. Chiappetti). We divided the observation into segments of the same 10 ks duration and fitted the combined LECS/MECS spectra with a quadratic function. For the *BeppoSAX* data, we also fitted the spectra with a curved–power-law model for comparison. The derived peak flux and peak energy from both models are listed in Table 3. In fitting the combined LECS/MECS spectra, the normalizations were allowed to vary independently, and the values in Table 3 were normalized to the MECS2 value. The fitting results show that although there is one less spectral fit parameter in the quadratic function, both models equally represent the observed spectra. In contrast to the combined *EUVE*/GIS data, there is no energy gap in the *BeppoSAX* data, which provides support that our assumed quadratic form is appropriate in estimating the peak location in the *EUVE*/GIS case. The derived peak flux and peak energy using both functions are similar, but we also note that the quadratic function gives a slightly lower peak energy than the curved–power-law function.

The derived peak flux and peak energy, assuming the quadratic model, for the *BeppoSAX* observations are shown in
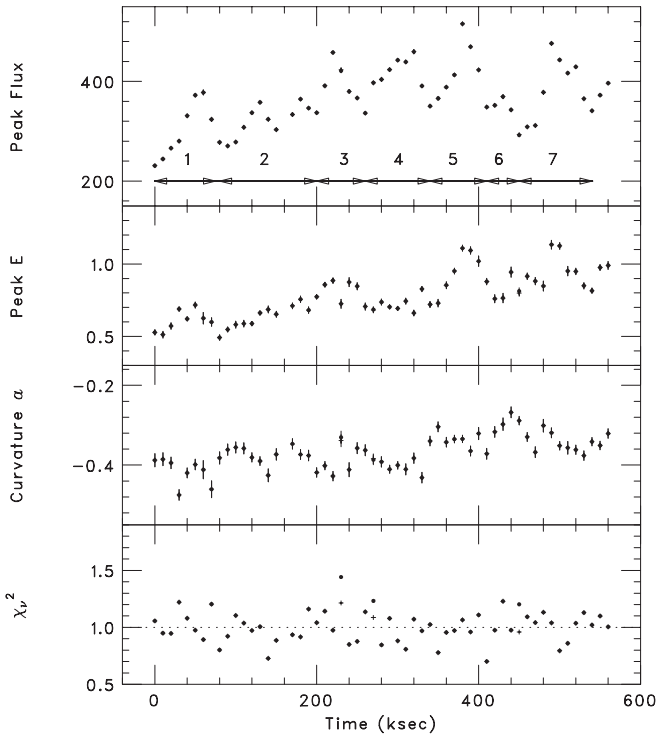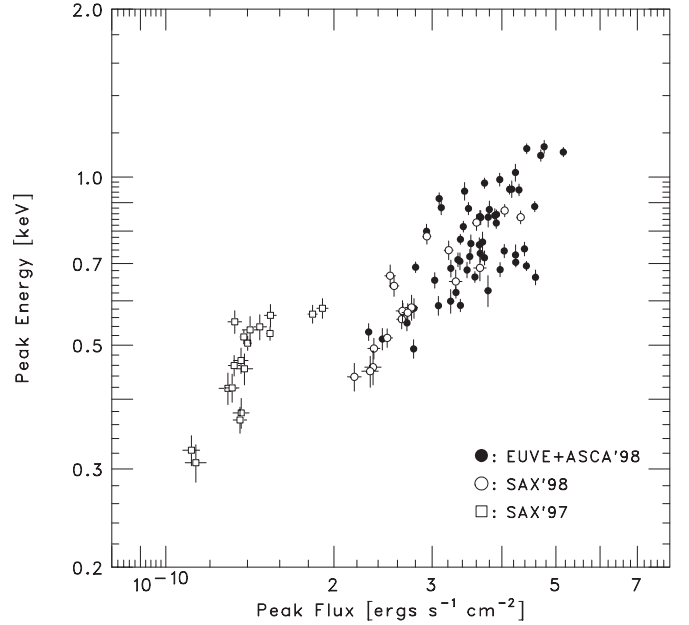

FIG. 2.—Time evolution of the spectrum fit parameters to the combined *EUVE* and *ASCA* spectra, assuming a quadratic function (see text): peak flux (*top*), peak energy (*second*), and curvature parameter (*third*; see definition in Table 1). The flux is in units of 10^{-12} ergs cm^{-2} s^{-1}, and peak energy is in keV. The bottom panel shows the reduced χ^2 for each of the fits. Three out of the 56 spectra showed a poor fit [$P(\chi^2) < 5\%$] due to several line or edgelike structures; the fit is significantly improved (*plus signs*) after excluding the energy ranges that included these structures.

TABLE 2

SPECTRAL FIT PARAMETERS FOR THE COMBINED *EUVE/ASCA* SPECTRA

Observation[a]	E_{peak} (keV)	$\nu F_{\nu, peak}$ (10^{-12} ergs cm^{-2} s^{-1})	a[b]	χ^2_ν (dof)
1................................	0.53 ± 0.02	230 ± 2	0.39 ± 0.02	1.06 (66)
2................................	0.51 ± 0.02	244 ± 3	0.39 ± 0.02	0.95 (85)
3................................	0.57 ± 0.02	266 ± 2	0.39 ± 0.01	0.95 (122)
4................................	0.69 ± 0.02	280 ± 2	0.48 ± 0.01	1.22 (106)
5................................	0.62 ± 0.01	331 ± 2	0.42 ± 0.01	1.08 (116)
6................................	0.72 ± 0.02	372 ± 2	0.40 ± 0.01	0.97 (137)
7................................	0.63 ± 0.04	377 ± 5	0.41 ± 0.02	0.89 (145)
8................................	0.60 ± 0.03	323 ± 4	0.46 ± 0.02	1.20 (87)
9................................	0.49 ± 0.02	277 ± 3	0.38 ± 0.02	0.80 (82)
10..............................	0.55 ± 0.02	270 ± 2	0.36 ± 0.01	0.92 (79)
11..............................	0.58 ± 0.02	278 ± 2	0.36 ± 0.01	1.10 (137)
12..............................	0.59 ± 0.02	307 ± 2	0.36 ± 0.01	1.04 (126)
13..............................	0.59 ± 0.02	337 ± 2	0.38 ± 0.01	0.97 (125)
14..............................	0.66 ± 0.02	358 ± 2	0.39 ± 0.01	1.01 (154)
15..............................	0.69 ± 0.02	324 ± 3	0.43 ± 0.02	0.73 (97)
16..............................	0.65 ± 0.02	303 ± 2	0.37 ± 0.01	0.89 (87)
18..............................	0.71 ± 0.02	333 ± 2	0.35 ± 0.01	0.93 (98)
19..............................	0.76 ± 0.02	364 ± 2	0.37 ± 0.01	0.92 (173)
20..............................	0.68 ± 0.02	346 ± 2	0.38 ± 0.01	1.16 (144)
21..............................	0.77 ± 0.02	337 ± 2	0.42 ± 0.01	1.04 (132)
22..............................	0.86 ± 0.02	391 ± 2	0.40 ± 0.01	1.14 (169)
23..............................	0.89 ± 0.02	458 ± 2	0.43 ± 0.01	0.97 (184)
24..............................	0.73 ± 0.03	423 ± 3	0.34 ± 0.02	1.21 (119)
25..............................	0.87 ± 0.03	379 ± 3	0.41 ± 0.02	0.85 (113)
26..............................	0.85 ± 0.02	366 ± 2	0.36 ± 0.01	0.88 (95)
27..............................	0.71 ± 0.02	336 ± 2	0.36 ± 0.01	1.14 (153)
28..............................	0.68 ± 0.02	397 ± 3	0.38 ± 0.01	1.09 (146)
29..............................	0.74 ± 0.02	404 ± 3	0.39 ± 0.01	0.85 (125)
30..............................	0.70 ± 0.01	423 ± 2	0.41 ± 0.01	1.08 (176)
31..............................	0.69 ± 0.01	442 ± 2	0.40 ± 0.01	0.88 (181)
32..............................	0.74 ± 0.02	439 ± 3	0.41 ± 0.01	0.81 (124)
33..............................	0.66 ± 0.02	459 ± 3	0.38 ± 0.01	1.07 (136)
34..............................	0.83 ± 0.02	390 ± 3	0.43 ± 0.01	0.97 (93)
35..............................	0.72 ± 0.02	350 ± 2	0.34 ± 0.01	1.02 (135)
36..............................	0.73 ± 0.03	365 ± 2	0.30 ± 0.01	0.78 (136)
37..............................	0.85 ± 0.02	388 ± 2	0.34 ± 0.01	0.96 (165)
38..............................	0.95 ± 0.02	413 ± 2	0.33 ± 0.01	0.97 (187)
39..............................	1.11 ± 0.02	515 ± 2	0.33 ± 0.01	1.07 (182)
40..............................	1.09 ± 0.03	469 ± 2	0.36 ± 0.01	0.96 (146)
41..............................	1.02 ± 0.04	423 ± 2	0.32 ± 0.02	1.11 (153)
42..............................	0.88 ± 0.02	348 ± 2	0.37 ± 0.01	0.70 (92)
43..............................	0.76 ± 0.03	352 ± 2	0.32 ± 0.01	0.98 (131)
44..............................	0.76 ± 0.03	369 ± 3	0.30 ± 0.02	1.23 (84)
45..............................	0.94 ± 0.03	343 ± 2	0.27 ± 0.01	0.98 (97)
46..............................	0.80 ± 0.02	293 ± 1	0.29 ± 0.01	0.96 (126)
47..............................	0.92 ± 0.02	308 ± 2	0.33 ± 0.01	1.09 (138)
48..............................	0.88 ± 0.03	311 ± 2	0.37 ± 0.01	1.04 (130)
49..............................	0.85 ± 0.03	378 ± 3	0.30 ± 0.02	1.13 (80)
50..............................	1.13 ± 0.03	476 ± 2	0.32 ± 0.01	1.04 (132)
51..............................	1.12 ± 0.02	443 ± 2	0.35 ± 0.01	0.79 (144)
52..............................	0.95 ± 0.03	416 ± 3	0.36 ± 0.02	0.86 (112)
53..............................	0.95 ± 0.02	429 ± 2	0.36 ± 0.01	1.04 (171)
54..............................	0.85 ± 0.02	365 ± 2	0.38 ± 0.01	1.13 (180)
55..............................	0.82 ± 0.02	341 ± 2	0.34 ± 0.01	1.02 (152)
56..............................	0.98 ± 0.02	372 ± 2	0.35 ± 0.01	1.10 (157)
57..............................	0.99 ± 0.03	396 ± 2	0.32 ± 0.01	1.00 (166)

NOTE.—All errors represent the 1 σ error.
[a] Each number represents the observation divided into 10 ks segments.
[b] See Table 1 for definition.

TABLE 3

Spectral Fit Parameters for the *BeppoSAX* Spectra

Date	Observation[a]	Quadratic				Curved Power Law		
		E_{peak} (keV)	$\nu F_{\nu,\,\text{peak}}$ (10^{-12} ergs cm^{-2} s^{-1})	a[b]	χ^2_ν (dof)	E_{peak} (keV)	$\nu F_{\nu,\,\text{peak}}$ (10^{-12} ergs cm^{-2} s^{-1})	χ^2_ν (dof)
1997 Apr 29......	1	0.54 ± 0.03	137 ± 3	0.48 ± 0.02	0.99 (126)	0.56 ± 0.02	146 ± 6	0.96 (125)
	2	0.46 ± 0.02	124 ± 2	0.48 ± 0.02	1.21 (126)	0.49 ± 0.02	125 ± 4	1.23 (125)
	3	0.50 ± 0.01	131 ± 2	0.46 ± 0.01	1.16 (126)	0.53 ± 0.01	134 ± 3	1.15 (125)
1997 Apr 30......	1	0.53 ± 0.03	132 ± 4	0.48 ± 0.02	1.24 (126)	0.55 ± 0.04	127 ± 5	1.25 (125)
	2	0.47 ± 0.02	127 ± 3	0.47 ± 0.02	0.88 (126)	0.50 ± 0.02	132 ± 5	0.85 (125)
	3	0.55 ± 0.03	124 ± 3	0.51 ± 0.02	0.85 (126)	0.58 ± 0.03	123 ± 4	0.84 (125)
	4	0.52 ± 0.01	129 ± 2	0.47 ± 0.01	0.81 (126)	0.55 ± 0.01	130 ± 2	0.79 (125)
1997 May 1.......	1	0.45 ± 0.03	129 ± 4	0.45 ± 0.02	1.11 (126)	0.48 ± 0.03	131 ± 6	1.11 (125)
	2	0.57 ± 0.03	144 ± 3	0.44 ± 0.02	1.03 (126)	0.59 ± 0.03	146 ± 4	1.03 (125)
	3	0.58 ± 0.02	178 ± 4	0.49 ± 0.02	0.84 (126)	0.61 ± 0.03	170 ± 5	0.85 (125)
	4	0.52 ± 0.01	143 ± 2	0.44 ± 0.01	1.03 (126)	0.55 ± 0.02	145 ± 2	1.01 (125)
1997 May 2.......	1	0.57 ± 0.03	171 ± 3	0.46 ± 0.01	0.86 (126)	0.60 ± 0.03	174 ± 4	0.85 (125)
1997 May 3.......	1	0.42 ± 0.03	120 ± 4	0.48 ± 0.02	0.97 (126)	0.39 ± 0.06	116 ± 4	0.96 (125)
	2	0.42 ± 0.02	123 ± 3	0.44 ± 0.02	1.13 (126)	0.41 ± 0.05	120 ± 4	1.14 (125)
1997 May 4.......	1	0.31 ± 0.02	105 ± 4	0.50 ± 0.03	1.23 (126)	0.22 ± 0.09	104 ± 5	1.25 (125)
	2	0.32 ± 0.02	103 ± 3	0.50 ± 0.02	1.23 (126)	0.32 ± 0.05	103 ± 4	1.24 (125)
1997 May 5.......	1	0.38 ± 0.02	127 ± 4	0.47 ± 0.02	1.24 (126)	0.42 ± 0.03	131 ± 5	1.24 (125)
	2	0.37 ± 0.02	127 ± 3	0.46 ± 0.02	1.24 (126)	0.40 ± 0.03	129 ± 4	1.25 (125)
1998 Apr 21–22...............	1	0.69 ± 0.04	341 ± 8	0.42 ± 0.02	1.04 (126)	0.69 ± 0.04	357 ± 13	1.01 (125)
	2	0.85 ± 0.02	404 ± 6	0.42 ± 0.01	1.12 (126)	0.93 ± 0.03	397 ± 7	1.06 (125)
	3	0.87 ± 0.02	378 ± 5	0.37 ± 0.01	1.03 (126)	0.91 ± 0.03	379 ± 6	1.04 (125)
	4	0.83 ± 0.03	337 ± 5	0.37 ± 0.01	0.93 (126)	0.87 ± 0.04	337 ± 7	0.94 (125)
	5	0.74 ± 0.03	300 ± 5	0.34 ± 0.01	0.90 (126)	0.72 ± 0.04	310 ± 7	0.86 (125)
	6	0.78 ± 0.03	274 ± 4	0.37 ± 0.01	1.31 (126)	0.82 ± 0.03	274 ± 5	1.33 (125)
	7	0.64 ± 0.03	239 ± 4	0.33 ± 0.02	1.04 (126)	0.68 ± 0.03	235 ± 5	1.02 (125)
	8	0.67 ± 0.03	236 ± 5	0.38 ± 0.02	0.95 (126)	0.70 ± 0.04	235 ± 6	0.96 (125)
1998 Apr 23–24...............	1	0.65 ± 0.03	309 ± 8	0.44 ± 0.02	1.11 (126)	0.70 ± 0.05	287 ± 8	1.06 (125)
	2	0.58 ± 0.03	257 ± 6	0.38 ± 0.02	1.07 (126)	0.62 ± 0.03	257 ± 8	1.08 (125)
	3	0.56 ± 0.02	247 ± 5	0.40 ± 0.02	0.90 (126)	0.58 ± 0.02	254 ± 7	0.88 (125)
	4	0.58 ± 0.03	248 ± 6	0.43 ± 0.02	1.04 (126)	0.61 ± 0.03	239 ± 7	1.01 (125)
	5	0.57 ± 0.02	253 ± 5	0.44 ± 0.02	0.86 (126)	0.60 ± 0.03	251 ± 7	0.87 (125)
	6	0.52 ± 0.02	233 ± 5	0.44 ± 0.02	1.17 (126)	0.53 ± 0.03	227 ± 6	1.18 (125)
	7	0.49 ± 0.02	220 ± 5	0.43 ± 0.02	1.34 (126)	0.51 ± 0.03	218 ± 6	1.36 (125)
	8	0.46 ± 0.03	219 ± 7	0.38 ± 0.02	1.07 (126)	0.44 ± 0.06	213 ± 8	1.08 (125)
	9	0.45 ± 0.03	217 ± 7	0.42 ± 0.02	1.04 (126)	0.34 ± 0.09	203 ± 7	1.01 (125)
	10	0.44 ± 0.03	203 ± 5	0.40 ± 0.02	1.14 (126)	0.39 ± 0.06	194 ± 6	1.14 (125)

Note.—All errors represent the 1 σ error.
[a] Each number represents the observation divided into 10 ks segments.
[b] See Table 1 for definition.

Figure 3 as the open circles (for 1998) and squares (for 1997). Note that the *BeppoSAX* data points in Figure 3 are multiplied by a normalization factor of 1.07, which we adopted from the combined fit in § 3.1 It can be seen that the results during the 1998 campaign lie on a slope similar to that for the results derived from the *EUVE*/GIS data during the same campaign.

The relation of peak flux $\nu F_{\nu,\,\text{peak}}$ and peak energy E_{peak} for the *EUVE*/GIS data set can be best described with a power-law function, $E_{\text{peak}} \propto \nu F^\alpha_{\nu,\,\text{peak}}$, where $\alpha = 0.72 \pm 0.02$ (or $\epsilon = 0.76 \pm 0.02$ in the form $E_{\text{peak}} \propto F^\epsilon_{0.1-10\,\text{keV}}$; see description below). Including also the *BeppoSAX* data points during 1998, the index becomes $\alpha = 0.77 \pm 0.02$ ($\epsilon = 0.72 \pm 0.02$). It can be seen that the data from 1997 lie on a somewhat different slope. The relation derived from the 1997 data *alone* gives $\alpha = 0.96 \pm 0.09$ ($\epsilon = 0.79 \pm 0.06$), slightly steeper than the index derived from the 1998 campaign. Fitting all the data

together, we obtain $\alpha = 0.59 \pm 0.01$ ($\epsilon = 0.50 \pm 0.01$). All errors correspond to a 1 σ error.

A similar analysis was performed by Fossati et al. (2000b) for the 1997 and 1998 *BeppoSAX* data. Fossati et al. (2000b) note a tight relationship between the measured integrated 0.1–10 keV flux $F_{0.1-10\,\text{keV}}$ and the peak energy E_{peak} such that $E_{\text{peak}} \propto F^\epsilon_{0.1-10\,\text{keV}}$, with $\epsilon = 0.55 \pm 0.05$, similar to the index derived from our results including all data sets. For a direct comparison, we fitted simultaneously the 1997 and 1998 data points for *BeppoSAX* only. This gave $\alpha = 0.52 \pm 0.02$ ($\epsilon = 0.45 \pm 0.01$). The estimated ϵ is slightly smaller than that reported in Fossati et al. (2000b), which might be the result of a different subdivision of the observations. Nonetheless, it is worth noting that the slope derived from the combined data appears be softer (smaller α or ϵ) than for each epoch considered alone.

Furthermore, the relation appeared to also vary between individual flares during the 1998 campaign. In some flares the peak energy clearly increases together with flux, while the correlation is weaker in others. This can be seen clearly in Figure 4, which shows the evolution of the synchrotron peak in each flare. The peak energy has a trend of shifting to the higher energy and then returning to the initial value together with the flux, but there is no common slope.

3.3. *Spectral Variations at Flares*

In the previous section, we described the spectral variations as the evolution of the location of the peak in the νF_ν spectrum. Here we take advantage of the wide energy range coverage afforded by the use of *EUVE*, *ASCA*, and *RXTE* data to investigate spectral variations in more detail. Given that the *RXTE* observations happen mostly during the flare minima rather than at their peaks (see Fig. 1 in Takahashi et al. 2000), here we focus on the beginning (rising portion) of the flares.

We divided the observations into 10 ks segments, as in § 3.2. For each segment, the GIS and PCA spectra are fitted simultaneously with a curved–power-law function, with an additional constant factor for the normalization. The derived source spectra in the GIS and PCA range are combined with the *EUVE* data points, which gives the total source spectrum in the energy range of $\sim$0.1–25 keV. In the top panels of Figures 5–7, we show the evolution of the νF_ν spectrum derived in this manner for the second, fourth, and fifth flares (starting from 80, 260, and 340 ks, respectively, as defined in Fig. 2). Note that the spectra are further rebinned for this figure. For each flare, we also plot a subsequent spectrum, but those only include the *EUVE* and GIS data.

To see the evolution more clearly, we calculated the ratio of the rebinned spectra by dividing these "subsequent" spectra by the spectrum measured at the onset of a given flare (integrated over 80–90, 260–270, and 340–350 ks, respectively). This is shown in the bottom panels of Figures 5–7. Interestingly, these three flares all showed different features. It can be seen that flare 2 starts with a hardening at the very highest energy range, with a concave shape in the ratio. As time progresses, the whole energy range becomes dominated by a new spectral slope. In contrast to this, in flare 4 the lower energy photons appear to precede the total flux rise. Flare 5 was similar to flare 2, but all energy bands increase together, with a larger amplitude at higher energies. We also studied the spectral variation for other flares, but a detailed investigation
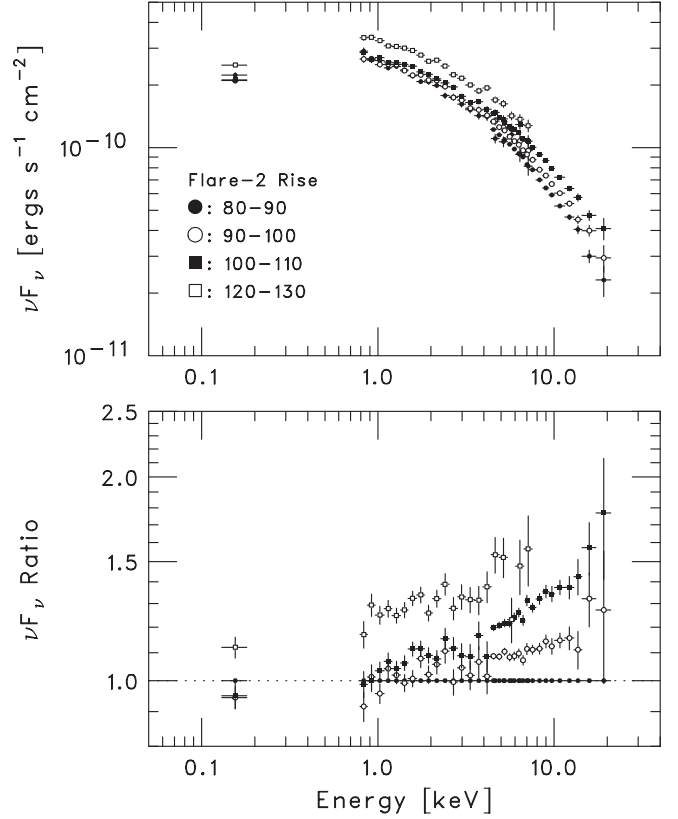

Fig. 5.—Spectral evolution during the rise of the second flare in the Mrk 421 observations during the 1998 campaign. The ratio of the subsequent spectrum to that at the onset of the rise is shown in the bottom panel. It can be seen that the flare starts with a hardening at the highest energy range, with a concave shape in the ratio that, with time, propagates down to the lower energies. In the last spectrum, which is 40 ks after the initial one, the whole spectrum is described with the new slope.

was rather difficult without a denser temporal coverage by *RXTE*.

3.4. *The X-Ray and TeV Correlation*

Since X-ray and TeV energies both reflect the electrons accelerated to the highest energies in TeV blazars, simultaneous X-ray and TeV observations provide an important tool for probing the emission region of the jet (e.g., Krawczynski,
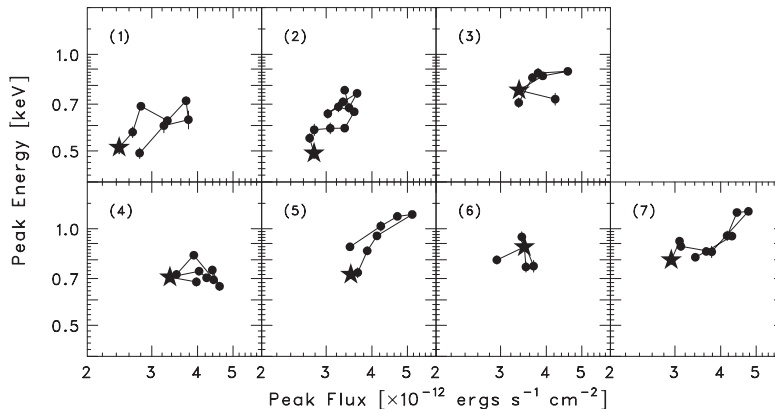

Fig. 4.—Time evolution of the correlation of the synchrotron peak flux $\nu F_{\nu,\,\mathrm{peak}}$ and peak energy E_{peak} for Mrk 421 during the 1998 campaign, plotted separately for each of the flares defined in Fig. 2. The initial value in each period is shown as a star, and the connecting line shows the time order. This figure illustrates that the relation of $\nu F_{\nu,\,\mathrm{peak}}$ and E_{peak} differs from flare to flare.
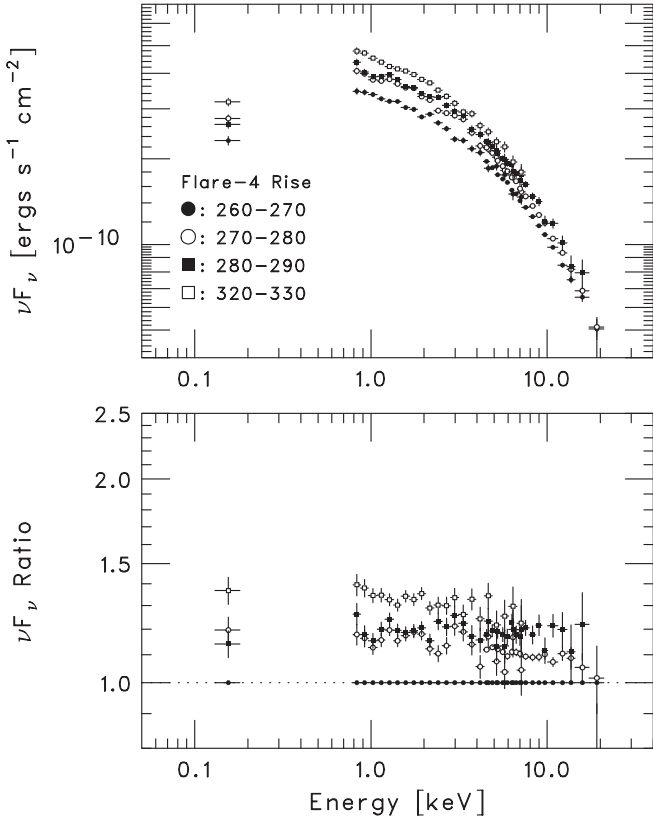
FIG. 6.—Same as Fig. 5, but for the fourth flare in the Mrk 421 observation during the 1998 campaign.

Coppi, & Aharonian 2002 and references therein). On the other hand, since blazars are highly variable on short time-scales, exactly simultaneous observations are essential. Thanks to the relatively high brightness of the source during the 1998 campaign, it was possible to generate a significant measurement for the separate TeV pointings every night (Aharonian et al. 1999; Takahashi et al. 2000). Here we provide the X-ray spectra from the exactly simultaneous time regions with the TeV observations.

For each TeV observation by HEGRA (Aharonian et al. 1999) and Whipple (Takahashi et al. 2000), we collected all existing X-ray data during the TeV exposure, from the *ASCA*, *RXTE*, and *EUVE* observations (the Coudé Auxiliary Telescope [CAT] observations mostly overlap with the HEGRA observations). In particular, all Whipple pointings during the *ASCA* observations happened to coincide with the *RXTE* observations, providing an X-ray spectrum ranging from 0.1–25 keV, simultaneous with the TeV observation.

We generated the combined X-ray spectrum using the same procedures described in §§ 3.2 and 3.3. We then fitted the X-ray spectrum for each period, assuming a quadratic function. The X-ray spectra during the HEGRA observations (consisting of the *EUVE* and *ASCA* data) are shown in Figure 8*a*. The spectrum for each observation is shown as a different symbol, and the dashed line shows the modeled quadratic function derived via the fit. The X-ray spectra during the Whipple observations, which consist of the *EUVE*, *ASCA*, and *RXTE* data, are shown in Figure 8*b*. Note that the spectra are further rebinned in the figures. While each integration time is as short as several hours, it can be seen that the curved shape of the high-energy peak of the synchrotron spectrum is clearly

resolved, and it is evident that the peak is located in the X-ray range.

The results of fits to each X-ray spectrum concurrent with the TeV pointings are summarized in Table 4. We also list the simultaneous TeV fluxes, for which the HEGRA data were taken by Aharonian et al. (1999). In Figure 9, we show the correlation of the derived location of the synchrotron peak flux with the TeV flux. Since the sensitive energy ranges of the two TeV telescopes are slightly different, we used the integrated flux in Crab units. A good correlation can be seen, showing that the TeV flux is higher when the synchrotron peak flux is higher. A best fit to the relation with a power-law function gives $F_{\text{TeV}} \propto F_{\text{sy, peak}}^{\alpha}$, with $\alpha = 1.7 \pm 0.3$.

4. SUMMARY AND DISCUSSION

We have performed detailed analysis of the combined *EUVE*, *ASCA*, *BeppoSAX*, and *RXTE* data collected during the long-look campaign of Mrk 421 in 1998, resulting in the measurement of the time-resolved spectrum in a broad energy range of 0.1–25 keV in segments as short as several ks. These are among the highest quality spectra with regard to both photon statistics and energy coverage so far for any blazar, providing the precise spectral shape at the highest energy end of the synchrotron spectrum.

We have shown that both a curved–power-law function and a quadratic function in $\log \nu - \log (\nu F_\nu)$ space reproduce the combined *EUVE*, *BeppoSAX*, *ASCA*, and *RXTE* spectrum. For the epochs at which *BeppoSAX* data do not exist, we assumed that the spectral gap between *EUVE* and *ASCA* can be extrapolated with a quadratic function, and we showed that the
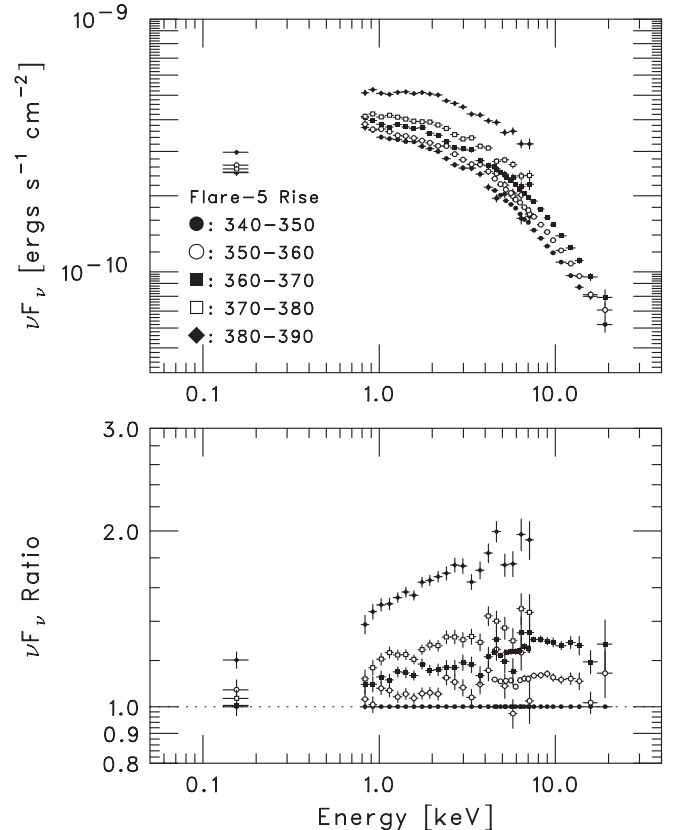

FIG. 7.—Same as Fig. 5, but for the fifth flare in the Mrk 421 observation during the 1998 campaign.
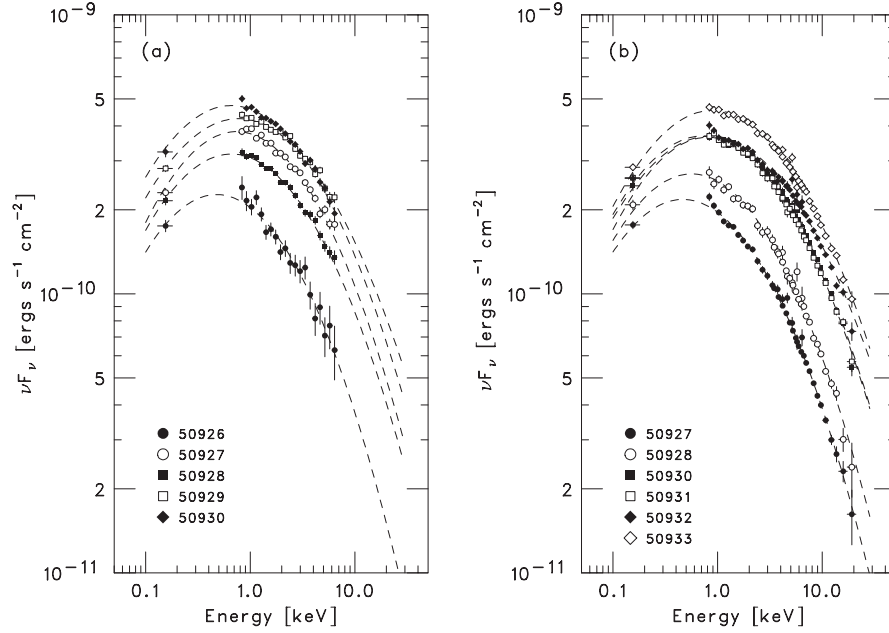
FIG. 8.—X-ray spectra of Mrk 421 obtained simultaneously with (a) HEGRA and (b) Whipple observations during the 1998 campaign. Each symbol corresponds to a different TeV observations, as shown in the key. The X-ray data include those collected by the *EUVE* and *ASCA* satellites for the HEGRA pointing and, in addition, those from the *RXTE* satellite for the Whipple observations, and they clearly show the curvature of the synchrotron spectrum.

energy and the flux at the synchrotron peak in the νF_ν spectrum are correlated, showing an overall trend of a higher synchrotron peak energy for higher peak flux, but the details of this relation differed from flare to flare. In particular, of the three flares, one started from a rise in the higher energy, while another started from a rise in the lower energy. The relative amplitude of the rise in different energies also differed from flare to flare. An interesting result was shown for the second flare, indicating that this flare started with a hardening at the higher energy. This feature is difficult to describe by a simple cooling or acceleration of a single electron distribution (see, e.g., Kataoka 2000), and thus this concave curvature indicates that two different spectral components were likely coexisting at the beginning of the flare. We remark that such a behavior is observed in only one flare, but the importance is that we

observed a flare that could not be explained by a single electron distribution. This suggests an appearance of a new component, which generated the observed flare.

Recently, many theoretical studies has been performed to model the energy dependence, or time lags, observed in the day-scale flares in blazars. One approach considers models with a homogeneous emission region (Mastichiadis & Kirk 1997; Chiaberge & Ghisellini 1999; Li & Kusunose 2000). For instance, Mastichiadis & Kirk (1997) have suggested that a sudden increase in the maximum energy of the accelerated electrons could result in the X-ray and TeV flare observed in Mrk 421. Similar results were shown by Kataoka et al. (2000), in reproducing the soft lag observed in PKS 2155−304. However, most of these models assume a change in some parameter in the emission region (such as the magnetic field,

TABLE 4
SIMULTANEOUS TeV FLUX AND SYNCHROTRON PEAK ENERGY AND FLUX FOR Mrk 421

		TeV		X-RAY			
START TIME (MJD)	DURATION (ks)	Observatory	TeV Flux (crab)	E_{peak} (keV)	$\nu F_{\nu,\,\mathrm{peak}}$ (10^{-12} ergs cm^{-2} s^{-1})	a^{a}	χ_ν^2 (dof)
50,926.8814.....	11.0	HEGRA	0.46 ± 0.10	0.48 ± 0.03	226 ± 6	0.45 ± 0.04	0.75 (33)
50,927.1390.....	13.7	Whipple	0.33 ± 0.09	0.47 ± 0.01	218 ± 2	0.42 ± 0.01	0.95 (216)
50,927.8839.....	10.5	HEGRA	0.79 ± 0.12	0.74 ± 0.02	381 ± 3	0.43 ± 0.01	1.18 (210)
50,928.2273.....	5.3	Whipple	0.33 ± 0.07	0.56 ± 0.02	269 ± 3	0.42 ± 0.01	0.95 (142)
50,928.8824.....	10.5	HEGRA	0.58 ± 0.10	0.66 ± 0.02	316 ± 2	0.41 ± 0.01	0.90 (221)
50,929.8848.....	10.1	HEGRA	1.10 ± 0.13	0.77 ± 0.02	424 ± 2	0.36 ± 0.01	1.13 (205)
50,930.1516.....	12.2	Whipple	0.54 ± 0.05	0.81 ± 0.02	364 ± 2	0.40 ± 0.01	0.99 (274)
50,930.8845.....	9.8	HEGRA	1.41 ± 0.15	0.66 ± 0.03	472 ± 4	0.39 ± 0.01	1.15 (244)
50,931.1467.....	10.3	Whipple	0.58 ± 0.14	0.72 ± 0.02	367 ± 3	0.38 ± 0.01	0.94 (229)
50,932.2041.....	6.9	Whipple	0.67 ± 0.07	$0.84 \pm\pm 0.02$	367 ± 2	0.34 ± 0.01	1.31 (239)
50,933.2358.....	3.4	Whipple	0.67 ± 0.11	0.90 ± 0.02	454 ± 2	0.38 ± 0.01	1.21 (238)

NOTE.—All errors represent the 1 σ error.
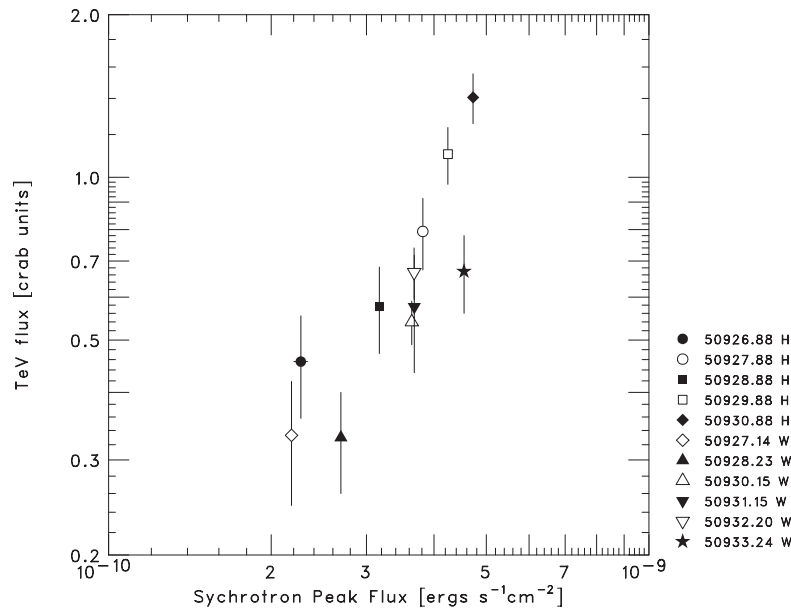[a] See Table 1 for definition.

Fig. 9.—Correlation of the synchrotron peak flux and the TeV flux (in Crab units) for the simultaneous observations of Mrk 421 during the campaign in 1998. The synchrotron peak flux is derived from observations by *EUVE* and *ASCA* (and *RXTE* for the Whipple pointings) during the exactly simultaneous epochs when the TeV data are available. The letters "H" and "W" denote HEGRA and Whipple pointings, respectively.

maximum energy of electrons, or number density of electrons). The observational results for Mrk 421 described above lead us to suggest a different scenario.

An alternative scenario has each flare forming as a result of a separate electron distribution. This was suggested in modeling the high-state spectral energy distribution (SED) of Mrk 501 (Kataoka et al. 1999). They applied the one-zone homogeneous synchrotron self-Compton model to the SED from 1997 April and concluded that a single electron distribution is insufficient to reproduce the observed synchrotron spectrum. This scenario could work, for instance, when the jet is emitted intermittently from the central engine and several separate regions generate different emission components. Another viable scenario can be provided by an internal-shock model, in which the light curve results from a superposition of many flares due to the collisions of shells, which may occur when a faster shell catches up to a slower shell (Ghisellini 2001; Spada et al. 2001; Sikora et al. 2001).

In fact, Tanihata et al. (2003) have shown from simulations that the internal-shock model can naturally explain various variability properties observed in TeV blazars. One observational fact is that the X-ray flares always appear to lie on top of an underlying offset-like component. In the internal-shock model, flares can be considered as arising from collisions of the shells that had the largest difference in initial velocity. All other collisions generate smaller amplitude, longer flares, which pile up to generate the offset component. In this case, it was shown that the flares will tend to have a higher synchrotron peak energy, as compared with that of the offset component.

Assuming that flares are due to an emergence of a new component with a higher synchrotron peak energy than the preexisting component, the synchrotron peak energy in the observed spectrum would appear as a shift to a higher energy. It is interesting to note that our observations are consistent with this, with the overall trend of the synchrotron peak energy being higher during flares. Furthermore, in this case, the spectral evolution would depend on the relation of the new and preexisting spectra. This would naturally explain the differing spectral evolution among different flares.

Finally, we remark again that because of the data gap between the *EUVE* and *ASCA* data in our observations, the results concerning the spectrum peak are somewhat tentative. Because of the rapid variability of the source on short timescales, the effective area of the instrument is most important. Long-look observations by the new observatories, such as *XMM-Newton*, should provide data allowing a more detailed analysis of the flaring mechanism, leading to the dynamics of the accelerated electrons in blazar jets.

REFERENCES

Aharonian, F. A., et al. 1999, A&A, 350, 757
Blandford, R. D., & Königl, A. 1979, ApJ, 232, 34
Burke, B. E., Mountain, R. W., Harrison, D. C., Bautz, M. W., Doty, J. P., Ricker, G. R., & Daniels, P. J. 1991, IEEE Trans. Electron Devices, 38, 1069
Chiaberge, M., & Ghisellini, G. 1999, MNRAS, 306, 551
Dermer, C. D., & Schlickeiser, R. 1993, ApJ, 416, 458

Dermer, C. D., Schlickeiser, R., & Mastichiadis, A. 1992, A&A, 256, L27
Elvis, M., Lockman, F. J., & Wilkes, B. J. 1989, AJ, 97, 777
Fiore, F., Guainazzi, M., & Grandi, P. 1999, Handbook for *BeppoSAX* NFI Spectral Analysis (Rome: ASI)
Fossati, G., et al. 2000a, ApJ, 541, 153
———. 2000b, ApJ, 541, 166

Gaidos, J. A., et al. 1996, Nature, 383, 319
Ghisellini, G. 2001, in ASP Conf. Ser. 227, Blazar Demographics and Physics, ed. P. Padovani & C. M. Urry (San Francisco: ASP), 85
Ghisellini, G., & Maraschi, L. 1989, ApJ, 340, 181
Jones, T. W., O'Dell, S. L., & Stein, W. A. 1974, ApJ, 188, 353
Kataoka, J. 2000, Ph.D. thesis, Univ. Tokyo
Kataoka, J., Takahashi, T., Makino, F., Madejski, G. M., Tashiro, M., Urry, C. M., & Kubo, H. 2000, ApJ, 528, 243
Kataoka, J., et al. 1999, ApJ, 514, 138
———. 2001, ApJ, 560, 659
Krawczynski, H., Coppi, P. S., & Aharonian, F. 2002, MNRAS, 336, 721
Li, H., & Kusunose, M. 2000, ApJ, 536, 729
Lin, Y. C., et al. 1992, ApJ, 401, L61
Macomb, D. J., et al. 1995, ApJ, 449, L99
Maraschi, L., et al. 1999, ApJ, 526, L81
Marshall, H. L., Fruscione, A., & Carone, T. E. 1995, ApJ, 439, 90
Mastichiadis, A., & Kirk, J. G. 1997, A&A, 320, 19
Ohashi, T., et al. 1996, PASJ, 48, 157

Petry, D., et al. 1996, A&A, 311, L13
Pian, E., et al. 1998, ApJ, 492, L17
Piron, F., et al. 2001, A&A, 374, 895
Punch, M., et al. 1992, Nature, 358, 477
Sikora, M., Begelman, M. C., & Rees, M. J. 1994, ApJ, 421, 153
Sikora, M., Błażejowski, M., Begelman, M. C., & Moderski, R. 2001, ApJ, 554, 1 (erratum 561, 1154)
Spada, M., Ghisellini, G., Lazzati, D., & Celotti, A. 2001, MNRAS, 325, 1559
Takahashi, T., et al. 2000, ApJ, 542, L105
Tanihata, C., Takahashi, T., Kataoka, J., & Madejski, G. M. 2003, ApJ, 584, 153
Tanihata, C., Urry, C. M., Takahashi, T., Kataoka, J., Wagner, S. J., Madejski, G. M., Tashiro, M., & Kouda, M. 2001, ApJ, 563, 569
Tavecchio, F., et al. 2001, ApJ, 554, 725
Urry, C. M., & Padovani, P. 1995, PASP, 107, 803
Yamashita, A., et al. 1997, IEEE Trans Nucl. Sci., 44, 847
Yaqoob, T., et al. 2000, ASCA GOF Calibration Memo ASCA-CAL-00-06-01, ver. 1.0 (Greenbelt: NASA)